Nanoscale resolution immersion scanning thermal microscopy

Peter D. Tovee and Oleg V. Kolosov.

Physics Department, Lancaster University, Lancaster, LA1 3BE, UK.

Corresponding Author; o.kolosov@lancaster.ac.uk

Keywords; scanning thermal microscopy, nanoscale imaging, liquid environment, immersion, graphene

Abstract:

Nanoscale thermal properties are becoming of extreme importance in modern nanotechnology – for processor chips and RF amplifiers dissipate increasing power on the length scale of few tens of nanometers[1-3], for thermoelectric materials[4], and for sensors and biosensors using nanoscale sized features[5,6]. While Scanning Thermal Microscopy (SThM) using locally heated nanoscale probes is known for its ability to map thermal properties of materials and devices with micro and nanoscale resolution[7-13], such probing in the liquid environment was perceived impossible up to now due to dominating heat dissipation from the heated probe into the surrounding liquid that would deteriorate spatial resolution[9]. Nonetheless, our recent theoretical analysis of SThM[14] applied to liquid environment showed that for some SThM probe design with resistive heater located near the tip apex, the thermal signal would be only moderately affected, by less than 50 % on immersion in a dodecane environment. More significantly, SThM spatial resolution, surprisingly, would remain unaffected, while the thermal contact between the tip apex and the studied sample beneficially improved eliminating detrimental effects of surface roughness.

Our experimental realization of such immersion SThM, or iSThM, confirmed analytical predictions, and here we report for the first time nanoscale SThM measurements of thermal conductivity of Ultra Large Scale Integration (ULSI) polymer-ceramic-metal interconnects[15,16]. We show that the full liquid immersion in iSThM provides superior thermal link between a probe tip and Al lead, while eliminating spurious presence of surface roughness and voids. iSThM studies of 45 nm thick graphite flakes allowed to significantly decrease spurious effects of tip-

surface contact area variations at the flake edge, ubiquitous in air SThM, allowing to explore the anisotropic nature of nanoscale thermal conductivity in graphene layers.[17] The full width at half maximum (FWHM) of the flake edge for in-air SThM was between 78 to 151 nm, while for iSThM the edge FWHM was 56 nm, demonstrating its superior lateral resolution not affected by the topographical features, in a good qualitative agreement with thermal modeling. We believe that iSThM provides a game changing platform for previously unfeasible non-contact nanoscale measurements of thermophysical properties of nanomaterials, including direct investigation of nanothermal effects in graphene based high power rechargeable batteries and supercapacitors[18], probing liquid phase catalytic phenomena, and exploring metabolism in biological systems[19,20].

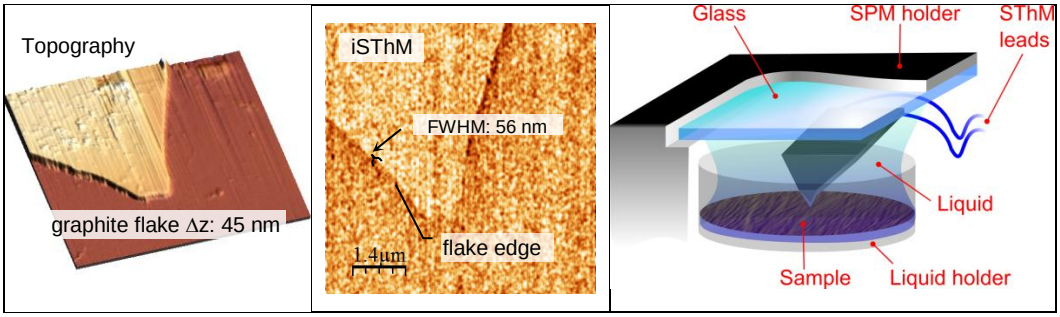

Since its invention, scanning probe microscopy (SPM)[21,22] became an indispensable tool in modern nanotechnology, allowing mapping of material surfaces with nanoscale resolution,[19] direct exploration of structure of nanoscale devices,[23,24] imaging of individual protein molecules[25] and atoms, including intramolecular electronic structure.[26] A significant advantage of SPM approaches is their ability to sense diverse physical and chemical properties of such structures with nanometer resolution,[27-30] including operation in various environments,[31-33] supporting and initiating novel nanotechnology developments. Among properties explored, nanoscale measurements of temperature[34,35], heat generation and nanoscale heat propagation are of increasing importance encouraged by continuous decrease of size of semiconductor devices with concurrent increase of processing power.[36] While SThM[7,8,37-39] that uses self-heated thermal sensors integrated with the sharp tip brought into contact with the studied sample, addresses some of these demands, one of major obstacles for SThM advances is the weak thermal coupling between sensor and the sample,[9] that, furthermore, fluctuates due to nanoscale sample geometry, that can drastically reduce performance of nanoscale thermal measurements.

It would be very tempting to use liquid immersion in SThM to improve both the thermal contact between the probe tip and the sample and contact uniformity, in an approach somewhat similar to one used in ultrasonic imaging where gel is used to achieve better acoustic coupling[40] or optical immersion where light reflection, refraction and scattering at the interfaces are minimized.[41] The only reported so far liquid immersion thermal approach is fluorescence thermometry[19], that so far showed only sub-micrometer range spatial resolution[42] and, being a passive method, incapable of measurements of local thermal transport and thermal conductivities. Such SThM liquid immersion could provide improved and stable thermal contact between the tip and the surface, compared to in-air or vacuum environment. Also, due to efficient heat transfer through liquid, it might be possible to perform truly non-contact scanning with the tip-surface separated by few nm gap, while retaining both nanoscale resolution and thermal sensitivity. Immersion SThM probe measurements, if available, would be also of extreme interest for biotechnology, where they will allow handling of delicate biological samples such as used in other SPM methods,[43-45] while mapping on nanoscale the heat of intermolecular interactions can help to explore functioning of molecular motors[46] and energy transfer in photosynthesis.[47] In industrial applications, it may open pathways for exploring nanoscale thermal phenomena in power batteries and fuel cells[48] as well as in chemistry in studies of nanoscale catalysts.[48]

Unfortunately until now such underliquid operation of SThM has been considered all but impossible[9] due to the potentially overwhelming direct heat dissipation from the heated sensor into the surrounding liquid, that would lead to degradation of lateral resolution. To our knowledge, there is so far no publication reporting such approach and measurements.

Notwithstanding the rationale described above, in this paper we simulated such immersion SThM, or iSThM, based on a widely used design of a SThM probe that is fully immersed in a liquid. [14] We found, surprisingly, that such measurements would not be qualitatively different from the operation in air or vacuum environment reported elsewhere.[13] Furthermore, we then

experimentally build such iSThM and demonstrated its capabilities on the system of polymer-ceramic-metal Ultra Large Scale Integration (ULSI) interconnects, as well as for 45 nm thick graphite flake on Si substrate, showing thermal mapping with 50 nm lateral resolution. The experimental results are then compared with the simulations, validating new physical phenomena observed in iSThM.

RESULTS AND DISCUSSION

SThM[7-9,12,49] is similar in many ways to the atomic force microscope (AFM).[22] In both, the tip is scanned across the sample surface in a raster way following its topography using a feedback loop that maintains a constant tip-surface force. The tip is Joule heated by passing a current through a resistive element near the tip apex. The probe design can vary from Wollaston wire (WW)[50] to Si_3N_4 microfabricated thermal probe with a thin Pd track (SP) as the tip heater[51] (Kelvin Nanotechnology) to microfabricated doped Si probe (Anasys Instruments) [38] (DS) and thermocouple junction probe[7,39]. The thermal resolution of the WW probe is about 1 μm whereas for microfabricated DS and SP probes it can be well below 100 nm.[13,52,53] As the tip is brought in contact with the surface the heat flows into the sample cooling the tip and, consequently, changing resistance of the sensor. Using a Maxwell bridge or similar measurement setup[14] (see Methods) the well-defined power can be applied to the sensor generating Joule heatwith the tip temperature measured simultaneously. As the tip is scanned across the sample, monitoring these values allows us to create a thermal image of the sample and to evaluate its local thermal resistance. [9,13,54]

Exploring the feasibility of iSThM. While the role of liquid film between the SThM tip apex is known to be essential[9-11,55] up to now there were no reports on heated SThM probes fully immersed in the liquid. So far SThM operation both in air and vacuum was demonstrated, with vacuum helping to eliminate heat dissipation through air.[39,53,13] At first glance, the direct heat dissipation from SThM probe to the surrounding liquid might result in the complete loss of sensitivity to the local sample thermal properties. Nevertheless, our preliminary simulations of SThM response using experimentally verified finite element analysis (FEA) model of the probe[14] for a widely used resistive SP probe showed only a moderate decrease in thermal signal (Fig, 1) while replacing air with dodecane. It can be seen that the highest temperature of SThM sensor is only slightly lower in liquid (35 degrees above ambient environment at 293 K) compared with air (54 degrees). More significantly, the spatial distribution of the temperature was strikingly similar in air and liquid (Fig. 1a, b) and the heat "plum" was located along the SThM tip rather that widely spread in the surrounding liquid (Fig. 1c), leading to lateral resolution of the probe not very different from one operating in air or vacuum. At the same time, thermal simulation of the Si based DS probe (with heater positioned at the base of the tip) did indicate significant deterioration of both thermal spatial resolution and sensitivity. The dodecane was selected as it is a low-volatility liquid with intermediate thermal conductivity and was non-corrosive to the particular SP sensor design. Additionally, our iSThM simulations showed that tip "hovering" above sample surface at 25 nm distance in liquid would still provide reasonable thermal contact

to the sample (with sensor temperatures readings close to the tip in direct contact with the sample at $\Delta z = 0$), whereas in air these reading are much more diverging (see Table 1 and Methods).

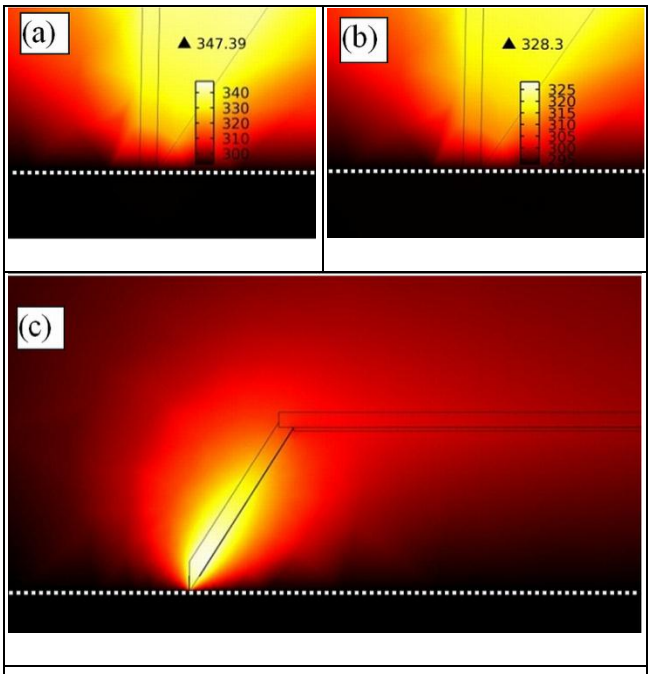

Figure 1. Finite elements simulations of in-air SThM and iSThM in dodecane. (a) In-air and (b) iSThM in dodecane in contact with Si sample. T_{max} – is the maximal temperature of the heater with respect to ambient temperature of 293 K, dotted lines indicate the sample surface. (c) Wider view of temperature distribution of SThM probe in contact with Si in dodecane.

Table 1. Simulation results of sensor temperature change ΔT while "hovering" ($\Delta z = 25$ nm) and retracted ($\Delta z = 200$ nm) tip, with respect to in-contact ($\Delta z = 0$) temperature; Si sample, air and dodecane environments.

Δz, nm	Air/ liquid	ΔT (mK)
$\Delta z = 0$ nm (contact)	Air	0

*Δz = 25 nm ("hovering" non-contact)	Air	45
Δz = 200 nm (retracted)	Air	99
Δz = 0 nm (contact)	Liquid	0
Δz = 25 nm ("hovering" non-contact)	Liquid	9
Δz = 200 nm (retracted)	Liquid	51
*Given that MFP in air of 50 nm, correction value for ΔT for "hovering" in air at Δz = 25 nm would further bring it closer to "non-contact" value of 99 mK		

We then created an analytical model of the SThM probe in order to estimate the influence of the heat loss to the environment, using equivalent axisymmetric probe (see Methods and Supplementary Fig. S1). Our analysis showed that probe thermal resistance for dodecane due to its higher thermal conductivity is approximately only twice lower than for an air environment, accounting for approximately 50 % drop of the probe signal, in line with the FEA analysis of the probe, and indicating that it would still provide sufficient response in iSThM measurements (see Methods).

Experimental realization of iSThM. Our iSThM was based on an AFM (Bruker Multi-Mode, Nanoscope III controller) modified for use with liquids and SThM (see Methods). For working under liquid a special PTFE holder was designed to contain the liquid with width sufficient to accommodate thermal cantilevers and connecting leads. A cantilever holder was additionally modified with glass window to create a flat glass-liquid interface for AFM laser beam monitoring cantilever deflection (Fig. 2a).

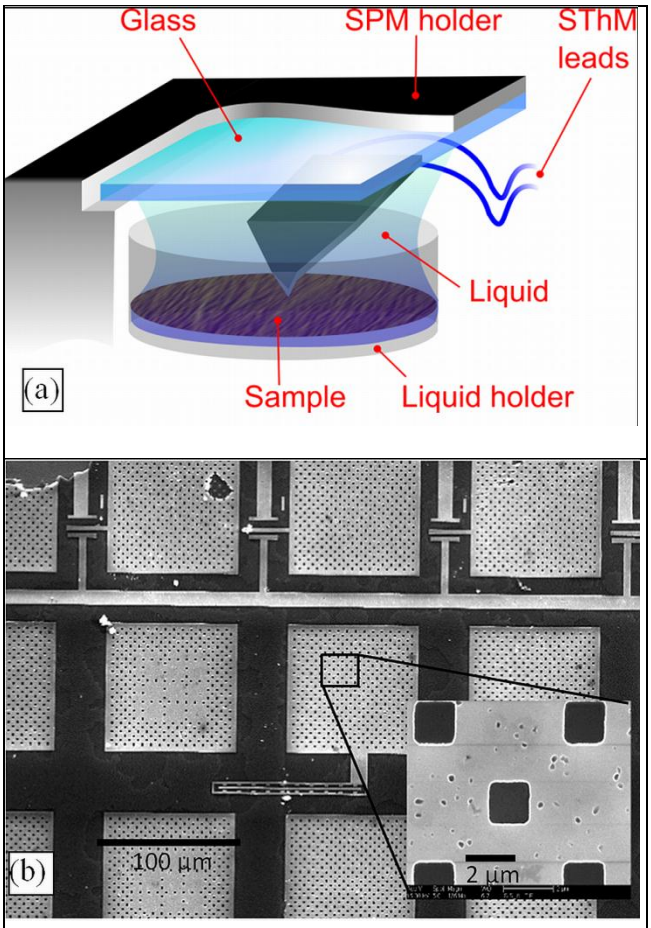

Figure 2. Experimental setup of iSThM and the SEM image of the test sample. (a) Diagram of AFM holder modified for use for under liquid SThM with glass plate to form a flat interface for laser beam monitoring the probe deflection, and a PTFE holder for the immersion liquid and a sample. (b) SEM image of Al - BCB (bensocyclobutene) polymer interconnects[15]; inset - higher magnification. Dark areas are the BCB polymer with the lighter grey areas the Al tracks, small voids at the Al grain boundaries are clearly visible.

To study the feasibility and performance of iSThM we used a test structure of chemo-mechanically polished damascene ultra large scale integration (ULSI) interconnects with Al tracks in a benzocyclobutene (BCB) polymer matrix on a Si wafer[15] (Fig. 2b). Heat transport in such nanostructures is of significant concern as these tracks in a real device carry significant

amount of current and their overheating would increase the electro-migration and adversely affect the stability of the ULSI device. Such structure also has a high (Al) and relatively low (BCB) thermal conductivity materials side-by-side with a well-defined boundaries that would allow to estimate both thermal sensitivity and resolution of SThM. The same sample was scanned first in air and then in dodecane to ensure no dodecane contamination has been left behind. SThM images in Fig. 3 were obtained with constant power applied to the sensor and resulting temperature recorded via measuring resistance variations of the sensor (see Methods). The higher heat transfer to the sample results in the lower sensor temperature and darker areas in the image; scan speed of about 0.4 Hz was used to produce clear thermal images. The air SThM image (Fig. 3b) clearly shows that the Al interconnects produce better heat dissipation from the tip corresponding to the lower thermal resistance. This is consistent with the higher thermal conductivity for Al, k_{Al} = 200 W/mK compared to BCB, k_{BCB} = 29 W/mK. The absolute topographical height (on the order of 100 nm) seemed to provide no direct influence for in-air thermal image, at the same time the edges of Al lead looked brighter (Fig. 3c) partly due to reduced area of the thermal contact at the rim. The increase of the heat transport was expected at the very edge of the flake (due to increased contact area of the side contact with SThM tip), but this was not observed, most likely due to roughness of the edge precluding efficient heat transport to the Al lead. The voids in Al filled with air (Fig. 3c) seem to create a barrier to the heat transport (increase in thermal resistance) resulting in "hotter" bright areas in SThM image.

iSThM was able to produce similar thermal contrast, of lower signal-to-noise ratio, with areas of Al interconnects revealing better heat dissipation (Fig. 3d). In contrast to in-air SThM, voids in Al did not produce significant increase in thermal resistance in iSThM, while a darker edge indicating higher heat transport to the side of Al lead was observed. These are clearly consistent with the fact that iSThM provided a better thermal contact to the studied sample, avoiding detrimental influence of nanoscale roughness, and providing important nanoscale thermal data.

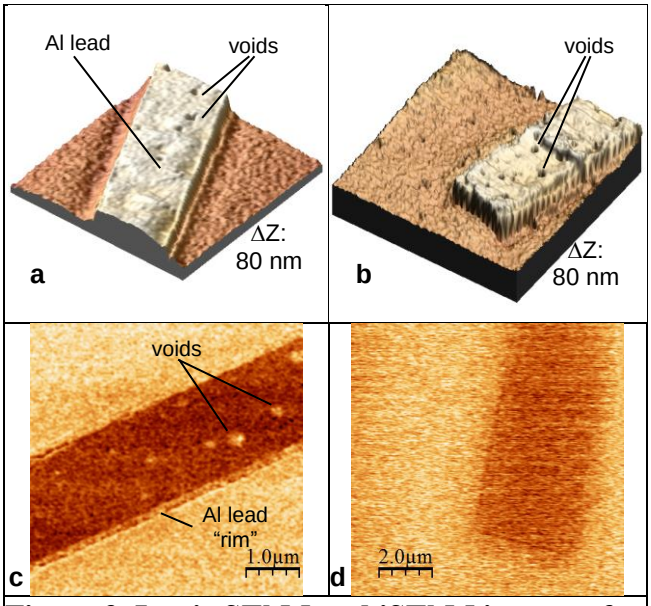

Figure 3. In-air SThM and iSThM images of

Al - BCB polymer interconnects sample. (a, b) Topographic height and (c, d) thermal signal. iSThM scans showing the height (b) and (c) thermal signal images of the different area of the same sample fully immersed in dodecane. For the constant heat generated by the probe, lower thermal resistance (higher local thermal conductivity) results in the lower temperature of the sensor, and therefore darker contrast. The height of Al lead ΔZ is shown in topography images. The darker areas in thermal images (c) and (d) are the Al tracks reflects the higher thermal conductivity of Al. For in-the-air SThM image (c) note the brighter contrast of the voids and the Al lead rim indicating decreased heat transport due to the surface roughness and defects, whereas iSThM thermal image (d) eliminates such detrimental effects, mainly reflecting the heat transport in this nanostructure.

In order to further analyze the performance of iSThM, we captured thermal signal and mechanical deflection of SThM sensor (proportional to force between the sample and SThM tip) as the tip approached the sample. Approach curves were carried out over Si sample with slow 0.01 Hz approach-retract rate. As the tip approaches the surface, the thermal signal decreases, as the heat is conducted to the sample cooling the probe. Once the solid-solid contact is established, the thermal signal remains constant even the force continue increasing, as reported elsewhere.[11]

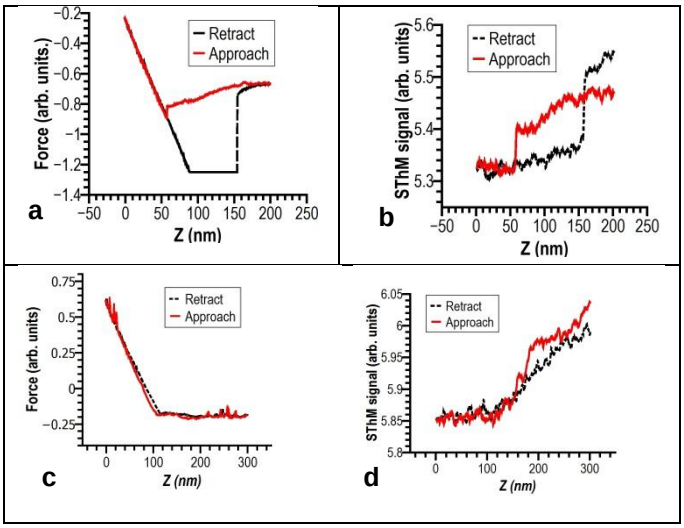

Figure 4. Experimental SThM approach-retract curves for Si sample. (a) force and (b) in-air SThM signal compared with (c) force and (d) iSThM signal in dodecane; approach-retract rate 0.01 Hz. Whereas there is a snap-in of cantilever in air (a) that is reflected in the jump in SThM response (b), there is neither force (c) nor observable SThM signal discontinuity while operating in liquid (d).

It is essential to note that in liquid iSThM there is no snap-in of tip to the sample due to attractive forces[56] that generally accompanies any AFM in-air measurements. That would allow to easily realize "hovering" of the SThM tip apex in the vicinity of the sample, while maintaining thermal contact between them during true non-contact imaging that can be realised, *e,g.* with shear force feedback[57]. From Fig. 4 it is clear that at longer distances both in air and in dodecane SThM signal depends on the distance between sample and the apex of the probe tip.

Once the iSThM approach was established, we have used iSThM to investigate thermal conductivity of anisotropic graphite nano-flake ($k_{\parallel\text{-}Gr\text{-}plane}$ = 2000 $Wm^{-1}K^{-1}$ $k_{\perp\text{-}Gr\text{-}plane}$ = 2 $Wm^{-1}K^{-1}$) of 42 ± 5 nm thickness on Si substrate (k_{Si} = 130 $Wm^{-1}K^{-1}$), comparing in-air and iSThM images (Fig. 5).

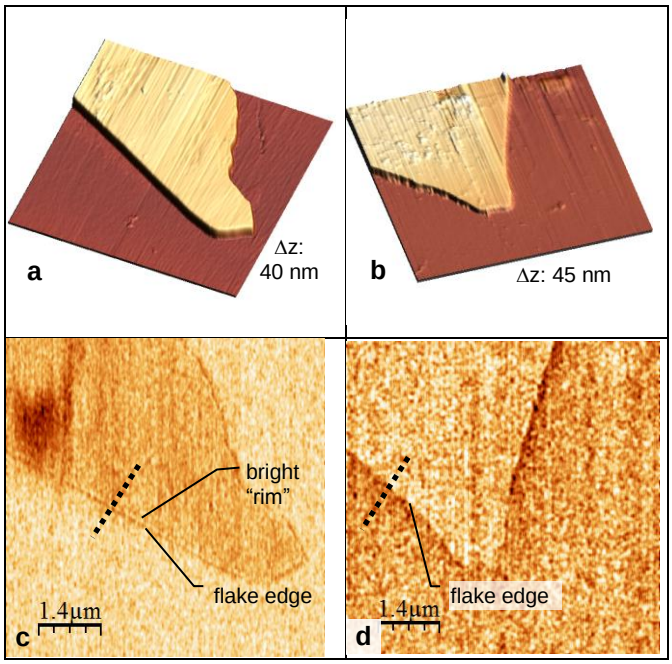

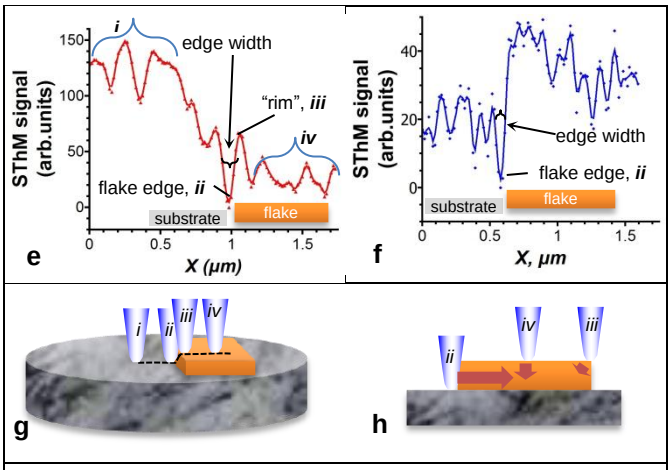

Figure 5. Nanoscale thermal transport in graphite flake. In-air topography (a) of 42 ± 5 nm nm thick graphite flake and (c) corresponding thermal image. (g, h) Schematic illustration of different regions in the images with SthM tip positioned on: ***i*** - the substrate, ***ii*** – beside edge of the flake (thermal contact area increased), ***iii*** – on the "rim" of the flake (contact area decreased), ***iv*** - on the flake area. (c) In-air SThM image and its profile and its 1D profile (e) (along dotted line in (c)) show the increased heat transport in the area of the flake (***iv***), and flake edge (***ii***) with strong decrease of heat transport at the flake rim (***iii***). At the same time, signal of underliquid iSThM (d) is not affected by the spurious "rim" contrast. The heat transport for on-the-flake position ***iv*** is slightly below one of Si (c.f. $k_{\perp\text{-}Gr\text{-}plane}$ of 2 $Wm^{-1}K^{-1}$ and k_{Si} of 130 $Wm^{-1}K^{-1}$), whereas side surface of the flake provide a better heat dissipation (tip position ***ii***) due to high in-plane conductivity of graphene layers ($k_{\parallel\text{-}Gr\text{-}plane}$ = 2000 $Wm^{-1}K^{-1}$) (h). The full width of half maximum (FWHM) of the flake edge for in-air SThM was 78 nm without the "rim" and 151 nm with the "rim" (e), and for iSThM the edge FWHM was 56 nm (f), demonstrating its superior lateral resolution not affected by the topographical features.

Fig. 5c,e shows that in-air SThM the heat transport is slightly increased in the area of the flake, and flake edge, with decrease of heat transport at the flake rim. At the same time, signal of underliquid iSThM (Fig. 5 d) is not affected by the spurious "rim" contrast, due to better thermal link between the tip and the sample not affected by the surface roughness. Moreover, the heat transport in the area of the flake (***iv***, as illustrated in the Fig. 5 g,h) is slightly below one of Si, as

one can expect that higher proportion of the heat flux normal to graphene layers (with relatively low thermal conductivity of graphite in direction perpendicular to graphene planes $k_{\perp\text{-}Gr\text{-}plane}$ of 2 $Wm^{-1}K^{-1}$ compared with thermal conductivity of Si - k_{Si} of 130 $Wm^{-1}K^{-1}$) contributing to the thermal conductivity of iSThM[56,58]. The side surface of the flake provides a better heat dissipation (tip position ***ii***) for both in-air and iSThM due to high in-plane conductivity of graphene layers ($k_{\parallel\text{-}Gr\text{-}plane}$ = 2000 $Wm^{-1}K^{-1}$). Although solid-solid contact area would increase at the flake edge, by comparison with ULSI interconnects, the direct topography influence on our probe (topographical variations in ULSI of 80 nm, significantly exceeding ones for graphite at 40 nm) attributing this phenomenon to mainly resulting from the extreme in-plane thermal conductivity of graphene layers contacted by the side of SThM probe, observed with minimal artefacts in iSThM.[56]

It is to be noted that the full width of half maximum (FWHM) of the flake edge for in-air SThM was 78 nm without the "rim" and 151 nm with the "rim" (e). At the same time, for iSThM the edge FWHM was only 56 nm (f), demonstrating its superior lateral resolution not affected by the topographical features.

In order to explore the clearly different nature of thermal contrast in ULSI interconnects of Al *vs* BCB, and of graphite flake on Si, we have performed FEA simulations of SThM line scans across Al/BCB boundary and graphite/Si edge and compared them with the experimentally measured line scans. Given that mean fee path for thermal transfer in liquids is on the order of 10 nm whereas distances and probe dimensions we are considering are of 50 nm or above, such approach was deemed appropriate[59,60].

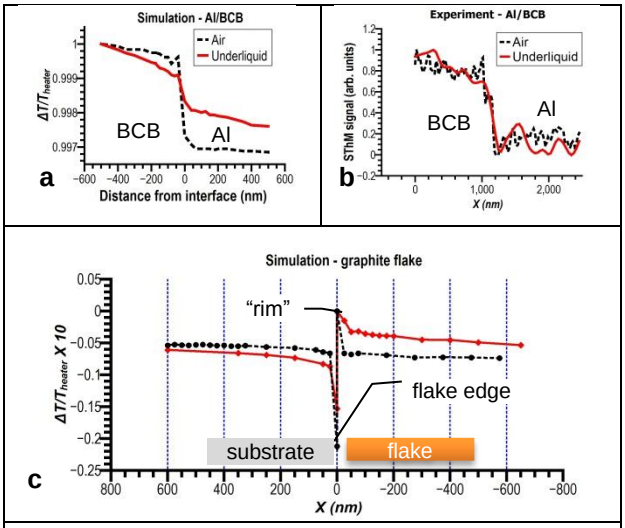

Figure 6. Simulated and experimentally measured in-air SThM and iSThM profiles. Sections (line scans) of thermal signal across the interface between Al and BCB polymer ((a) – simulation, (b) - experiment) shows good qualitative correspondence with lower temperature

(larger heat flux) for Al, and lateral thermal resolution on the order of 50-100 nm. Simulated SThM profiles (c) show increased heat transport for in-air SThM in the flake compared to Si substrate due to larger contribution of in-plane thermal conductivity for diverging flux. The higher heat transport at the flake edge is seen in both in-air and iSThM profiles, but is masked by the significant reduction of heat transport in the "rim" position for in-air SThM, that exceeds the differences between substrate and flake areas. At the same time, the underliquid iSThM profile shows the "rim" effect significantly reduced, with differences of heat transport in the flake and substrate perpendicular graphene planes clearly seen. The sign of the heat transport differences matches well with the ones experimentally observed in Fig. 5e,f.

Results of our simulations show that the SThM signal on the Al – BCB polymer boundary (Fig. 6a) does change appreciably over approximately 50 nm lateral distance, in good correlation with the experimental results (Fig. 6b) and the difference in thermal conductivities between Al and BCB. In dodecane this transition is smaller in amplitude however still provides similar lateral resolution of about 50 nm. For graphite nanoflake, the simulation provided additional support to our experimental finding, suggesting a drop of the SThM signal at the very edge of the flake, and small difference of SThM signal on the top of the flake compared with Si substrate. The higher heat transport at the flake edge is seen in both in-air and iSThM profiles, but is masked by the significant reduction of heat transport in the "rim" position for in-air SThM, that exceeds the differences between substrate and flake areas. At the same time, the underliquid iSThM profile shows the "rim" effect significantly reduced, with differences of heat transport in the flake and substrate perpendicular graphene planes clearly seen. The sign of the heat transport differences matches well with the ones experimentally observed in Fig. 5e,f..

CONCLUSION

In conclusion, we have demonstrated for the first time that SThM in fully immersed liquid environment is fully viable and can achieve nanoscale thermal resolution in samples with spatially inhomogeneous thermal conductivity, significantly reducing the roughness and contact area artifacts that often obscure the in-air SThM measuerements. New immersion SThM

(iSThM) provides superior thermal contact of the nanoscale probe and studied sample, allowing thermal mapping of ultra large scale integration Al - low-*k* BCB polymer interconnects and graphite nanoflakes on Si substrate, showing the anisotropic nature of nanoscale thermal conductivity in graphene layers. While the effective lateral resolution of the in-air SThM for 45 nm thick graphite nanoflake was reduced to 150 nm due to topographical artifacts, lateral resolution of iSThM for heat transport was 56 nm. The probe thermal response was shown to be in good qualitative agreement with analytical estimates as well as finite elements simulations, confirming the nanoscale resolution and sensitivity of iSThM. Future work may involve new probe designs tailored for iSThM, non-contact nanoscale measurements of thermal transport, optimization of operating parameters of the probe, and development of probes capable of working in polar liquids like water or electrolytes for new biomedical and energy storage applications.

MATERIALS AND METHODS

Finite elements (FE) modeling. The FE simulations were based on commercial COMSOL Multiphysics software package with two components, an AC/DC module modeling the current flow and Joule heating of the probe and a thermal module modeling the heat transport in the 3D probe geometry (see Supplementary Note 1). FE models were tested by varying mesh dimensions and the size of the cell, with results varying by less than 1 % indicating the adequate FE setup. As the MFP in liquid as well as in relevant materials in the models on the order of 10-25 nm, the diffusive approximation was also appropriate[13].

Analytical model of iSThM. We consider that the base of the thin triangular shaped Si_3N_4 probe of width w_c is effectively thermally anchored to the ambient temperature via thick highly thermally conductive Au leads[14]. Secondly, we take into account that the resistive heater, that is also a temperature sensing element, is evenly distributed along the length of the probe L_c. Finally, the heat transfer to the base of the probe is directed along the Si_3N_4 sheet of thickness t_c, whereas heat loss to the environment is predominantly normal to this sheet. The thermal resistance of the probe to the base can then be estimated as $R_b = \Delta T/Q = \left(t_C k w_c / L_c\right)^{-1}$ where k is thermal conductivity of the probe material, ΔT is probe temperature increase and Q is Joule heat generated in the probe. The thermal resistance of the probe to the ambient media (air or liquid) can then be estimated $R_m = \sqrt{1 - w_c/\left(2\pi L_c\right)} \Big/ 2\pi k_m L$ where k_m is thermal conductivity of the media (see Supplementary Note 2). As these thermal resistances act in parallel, the total thermal resistance R_t is determined[9,13] as $R_t = R_b R_m/(R_b + R_m)$. Substituting values for our probe (L_C = 10 μm, thermal conductivity for sputtered Si_3N_4 $k_{Si3N4} \approx 4$ W/mK, k_{air} = 0.025 W/mK, $k_{dodecane}$ = 0.14 W/mK) we obtain the estimate of the thermal resistance of the tapered end of the SThM probe as 1.0×10^5 K/W in the air and in dodecane of 0.56×10^5 K/W.

Experimental setup of SThM and calibration of thermal measurements. The SP thermal probe was calibrated on a Peltier hot/cold plate (Torrey Pines Scientific, Echo Therm model IC20) at several temperatures from room temperature to 80 ^{0}C and its electrical resistance

measured. During measurements and imaging the probe was included either as a part of a voltage divider in series with the fixed resistor, or a part of Maxwell electric bridge. The probe AC signal response was calibrated using the lock-in amplifier (Stanford Research Systems SRS-830) with a small applied voltage 2V AC voltage at 91 kHz for detection but small enough not to heat the tip. The voltage excitation for all measurements was provided by the precision function generator (Keithley 3390 50 MHz arbitrary waveform generator)[14]. As these calibrations took place outside the AFM so there was no heating affects from the laser. All calibrations were done both in air and then in dodecane with a period of few minutes for the dodecane to stabilize in temperature before each measurement. In the measurement voltage divider mode a multimeter (Agilent 34401A 6.5 digits precision) allowed measurement of the resistance of the probe as a function of the voltage at the probe which in turn allowed us to find temperature (see electronics setup for experimental measurements in Supplementary Fig. S3). In the measurements, Maxwell bridge configuration, the bridge was balanced at room temperature and absence of AFM laser illumination using variable resistor and capacitors before each calibration and before imaging. The imaging was done at low set force to minimize the risk of tip damage or breaking. A piece cut from a nitrile rubber glove was used underneath the liquid holder to protect the AFM scanner from accidental liquid spilling, however this needed to be changed from time to time as the dodecane placticises the rubber over the time. During scanning in liquid, a higher heating voltage, about 7 V_{DC} and $3V_{pp}$ AC had to be applied in order to compensate for higher heat dissipation in the liquid. This allowed to reach probe temperature similar to one obtained during the operation in air. Force setpoint was kept low and the scanning rate was 0.5 Hz for most operations with the lock-in response set to 3 ms. The cantilevers bases were modified so that they were tilted at a slightly shallower angle as to reflect the AFM laser back into the photodiode. The laser was aligned after the immersion in liquid and deflection zeroed at several points during the operation underliquid, including just before tip approach.

Samples preparation. ULSI interconnects were cleaned by 10 min sonication consecutively in acetone, ethanol, and DI water, and finally plasma cleaned in O_2/Ar plasma for 5 minutes to remove any residual organic contaminants on the surface. The graphene flake was deposited on Si wafer with 300 nm of SiO_2 thermal oxide that allowed the graphene to be seen in an optical microscope for area identification. The wafer was cleaned similar to the ULSU sample. The graphene was produced by mechanical exfoliation from graphite flakes using pressure sensitive tape.[61] The final exfoliation was done by cross-linked polymer gel (Gel-Pak, USA) to minimize tape residue transfer.

Acknowledgments

Authors acknowledge input of Manuel Pumarol for advice, scientific discussions and support related to the variety of aspects of SThM operation. We would like to thank Riccardo Mazzocco for his help with some of the paper's illustrations. We are also grateful to Hubert Pollock, Olaug Grude, and late Azeddine Hammiche for insight in using SThM, Bob Geer for providing ULSI samples, as well as Bob Jones for SEM analysis of the SP probes. OVK acknowledges support

from the EPSRC grants EP/G015570/1, EPSRC-NSF grant EP/G06556X/1 and EU FP7 GRENADA and FUNPROBE grants. We would also like to thank the group that produced WSxM for their useful program for analysis of SPM images.[62]

Additional information.

Supplementary Information accompanies this paper.

References:

1 Wang, L. & Li, B. Thermal logic gates: Computation with phonons. *Physical Review Letters* **99**, doi:10.1103/PhysRevLett.99.177208 (2007).
2 Ioffe, Z. *et al.* Detection of heating in current-carrying molecular junctions by Raman scattering. *Nature Nanotechnology* **3**, 727-732, doi:10.1038/nnano.2008.304 (2008).
3 Chen, G. & Shakouri, A. Heat transfer in nanostructures for solid-state energy conversion. *Journal of Heat Transfer-Transactions of the Asme* **124**, 242-252, doi:10.1115/1.1448331 (2002).
4 Snyder, G. J. & Toberer, E. S. Complex thermoelectric materials. *Nat. Mater.* **7**, 105-114, doi:10.1038/nmat2090 (2008).
5 Vetrone, F. *et al.* Temperature Sensing Using Fluorescent Nanothermometers. *Acs Nano* **4**, 3254-3258, doi:10.1021/nn100244a (2010).
6 Liu, W. & Asheghi, M. Phonon-boundary scattering in ultrathin single-crystal silicon layers. *Applied Physics Letters* **84**, 3819-3821, doi:10.1063/1.1741039 (2004).
7 Williams, C. C. & Wickramasinghe, H. K. SCANNING THERMAL PROFILER. *Applied Physics Letters* **49**, 1587-1589 (1986).
8 Nonnenmacher, M. & Wickramasinghe, H. K. SCANNING PROBE MICROSCOPY OF THERMAL-CONDUCTIVITY AND SUBSURFACE PROPERTIES. *Applied Physics Letters* **61**, 168-170 (1992).
9 Majumdar, A. Scanning thermal microscopy. *Annu. Rev. Mater. Sci.* **29**, 505-585 (1999).
10 Shi, L., Plyasunov, S., Bachtold, A., McEuen, P. L. & Majumdar, A. Scanning thermal microscopy of carbon nanotubes using batch-fabricated probes. *Applied Physics Letters* **77**, 4295-4297 (2000).
11 Shi, L. & Majumdar, A. Thermal transport mechanisms at nanoscale point contacts. *Journal of Heat Transfer-Transactions of the Asme* **124**, 329-337, doi:10.1116/1.1447939 (2002).
12 Tsukruk, V. V., Gorbunov, V. V. & Fuchigami, N. Microthermal analysis of polymeric materials. *Thermochim. Acta* **395**, 151-158 (2003).
13 Pumarol, M. E. *et al.* Direct Nanoscale Imaging of Ballistic and Diffusive Thermal Transport in Graphene Nanostructures. *Nano Letters* **12 (6)**, 2906–2911, doi:10.1021/nl3004946 (2012).
14 Tovee, P., Pumarol, M. E., Zeze, D. A., Kjoller, K. & Kolosov, O. Nanoscale spatial resolution probes for Scanning Thermal Microscopy of solid state materials. *J. Appl. Phys.* **112**, 114317 (2012).
15 Geer, R. E., Kolosov, O. V., Briggs, G. A. D. & Shekhawat, G. S. Nanometer-scale mechanical imaging of aluminum damascene interconnect structures in a low-dielectric-constant polymer. *Journal of Applied Physics* **91**, 4549-4555 (2002).

16 Shekhawat, G. S. & Dravid, V. P. Nanoscale imaging of buried structures via scanning near-field ultrasound holography. *Science* **310**, 89-92, doi:10.1126/science.1117694 (2005).
17 Balandin, A. A. Thermal properties of graphene and nanostructured carbon materials. *Nat. Mater.* **10**, 569-581, doi:10.1038/nmat3064 (2011).
18 Vivekchand, S. R. C., Rout, C. S., Subrahmanyam, K. S., Govindaraj, A. & Rao, C. N. R. Graphene-based electrochemical supercapacitors. *Journal of Chemical Sciences* **120**, 9-13, doi:10.1007/s12039-008-0002-7 (2008).
19 Okabe, K. *et al.* Intracellular temperature mapping with a fluorescent polymeric thermometer and fluorescence lifetime imaging microscopy. *Nature communications* **3**, doi:10.1038/ncomms1714 (2012).
20 Hu, Z. Y., Thundat, T. & Asme. *Nanoscale energy conversion by using nano-catalytic particles*. (2006).
21 Binnig, G., Rohrer, H., Gerber, C. & Weibel, E. Tunneling through a controllable vacuum gap. *Applied Physics Letters* **40**, 178-180 (1982).
22 Binnig, G., Quate, C. F. & Gerber, C. Atomic force microscope. *Physical Review Letters* **56**, 930-933 (1986).
23 Balke, N., Bonnell, D., Ginger, D. S. & Kemerink, M. Scanning probes for new energy materials: Probing local structure and function. *Mrs Bulletin* **37**, 633-637, doi:10.1557/mrs.2012.141 (2012).
24 Dinelli, F. *et al.* Mapping surface elastic properties of stiff and compliant materials on the nanoscale using ultrasonic force microscopy. *Philosophical Magazine A, Physics of Condensed Matter Structure Defects and Mechanical Properties* **80**, 2299-2323 (2000).
25 Patil, S., Martinez, N. F., Lozano, J. R. & Garcia, R. Force microscopy imaging of individual protein molecules with sub-pico Newton force sensitivity. *J. Mol. Recognit.* **20**, 516-523, doi:10.1002/jmr.848 (2007).
26 Gross, L., Mohn, F., Moll, N., Liljeroth, P. & Meyer, G. The Chemical Structure of a Molecule Resolved by Atomic Force Microscopy. *Science* **325**, 1110-1114, doi:10.1126/science.1176210 (2009).
27 Butt, H. J., Cappella, B. & Kappl, M. Force measurements with the atomic force microscope: Technique, interpretation and applications. *Surf. Sci. Rep.* **59**, 1-152, doi:10.1016/j.surfrep.2005.08.003 (2005).
28 Benstetter, G., Biberger, R. & Liu, D. P. A review of advanced scanning probe microscope analysis of functional films and semiconductor devices. *Thin Solid Films* **517**, 5100-5105, doi:10.1016/j.tsf.2009.03.176 (2009).
29 Kolosov, O., Gruverman, A., Hatano, J., Takahashi, K. & Tokumoto, H. NANOSCALE VISUALIZATION AND CONTROL OF FERROELECTRIC DOMAINS BY ATOMIC-FORCE MICROSCOPY. *Physical Review Letters* **74**, 4309-4312, doi:10.1103/PhysRevLett.74.4309 (1995).
30 Kolosov, O. V. *et al.* Imaging the elastic nanostructure of Ge islands by ultrasonic force microscopy. *Physical Review Letters* **81**, 1046-1049 (1998).
31 Garcia, R. & Perez, R. Dynamic atomic force microscopy methods. *Surf. Sci. Rep.* **47**, 197-301, doi:10.1016/s0167-5729(02)00077-8 (2002).
32 Lee, J., Liao, A., Pop, E. & King, W. P. Electrical and Thermal Coupling to a Single-Wall Carbon Nanotube Device Using an Electrothermal Nanoprobe. *Nano Letters* **9**, 1356-1361, doi:10.1021/nl803024p (2009).

33 Seol, J. H. *et al.* Two-Dimensional Phonon Transport in Supported Graphene. *Science* **328**, 213-216, doi:10.1126/science.1184014 (2010).
34 Dobson, P. S., Mills, G. & Weaver, J. M. R. Microfabricated temperature standard based on Johnson noise measurement for the calibration of micro- and nano-thermometers. *Review of Scientific Instruments* **76**, doi:10.1063/1.1899463 (2005).
35 Aigouy, L., Tessier, G., Mortier, M. & Charlot, B. Scanning thermal imaging of microelectronic circuits with a fluorescent nanoprobe. *Applied Physics Letters* **87**, doi:10.1063/1.2123384 (2005).
36 Kalinin, S. V. & Bonnell, D. A. Screening phenomena on oxide surfaces and its implications for local electrostatic and transport measurements. *Nano Letters* **4**, 555-560, doi:10.1021/nl0350837 (2004).
37 Majumdar, A., Carrejo, J. P. & Lai, J. THERMAL IMAGING USING THE ATOMIC FORCE MICROSCOPE. *Applied Physics Letters* **62**, 2501-2503, doi:10.1063/1.109335 (1993).
38 Chui, B. W. *et al.* Low-stiffness silicon cantilevers for thermal writing and piezoresistive readback with the atomic force microscope. *Applied Physics Letters* **69**, 2767-2769, doi:10.1063/1.117669 (1996).
39 Kim, K., Jeong, W. H., Lee, W. C. & Reddy, P. Ultra-High Vacuum Scanning Thermal Microscopy for Nanometer Resolution Quantitative Thermometry. *Acs Nano* **6**, 4248-4257, doi:10.1021/nn300774n (2012).
40 Prokop, A. F. *et al.* Polyacrylamide gel as an acoustic coupling medium for focused ultrasound therapy. *Ultrasound in Medicine and Biology* **29**, 1351-1358, doi:10.1016/s0301-5629(03)00979-7 (2003).
41 Brakenhoff, G. J., Blom, P. & Barends, P. CONFOCAL SCANNING LIGHT-MICROSCOPY WITH HIGH APERTURE IMMERSION LENSES. *J. Microsc.-Oxf.* **117**, 219-232 (1979).
42 Aigouy, L., Lalouat, L., Mortier, M., Low, P. & Bergaud, C. Note: A scanning thermal probe microscope that operates in liquids. *Review of Scientific Instruments* **82**, doi:10.1063/1.3567794 (2011).
43 Hansma, H. G. *et al.* Properties of biomolecules measured from atomic force microscope images: A review. *J. Struct. Biol.* **119**, 99-108, doi:10.1006/jsbi.1997.3855 (1997).
44 Geringer, V. *et al.* Intrinsic and extrinsic corrugation of monolayer graphene deposited on SiO(2). *Physical Review Letters* **102**, doi:076102

10.1103/PhysRevLett.102.076102 (2009).
45 Zhang, Y., Dobson, P. S. & Weaver, J. M. R. High temperature imaging using a thermally compensated cantilever resistive probe for scanning thermal microscopy. *J. Vac. Sci. Technol. B* **30**, doi:10.1116/1.3664328 (2012).
46 Parmeggiani, A., Julicher, F., Ajdari, A. & Prost, J. Energy transduction of isothermal ratchets: Generic aspects and specific examples close to and far from equilibrium. *Physical Review E* **60**, 2127-2140, doi:10.1103/PhysRevE.60.2127 (1999).
47 Gust, D., Moore, T. A. & Moore, A. L. Mimicking photosynthetic solar energy transduction. *Accounts Chem. Res.* **34**, 40-48, doi:10.1021/ar9801301 (2001).
48 Zhang, Y. J. *et al.* A simple method to synthesize nanowires. *Chemistry of Materials* **14**, 3564-3568, doi:10.1021/cm0201697 (2002).
49 Pollock, H. M. & Hammiche, A. Micro-thermal analysis: techniques and applications. *Journal of Physics D-Applied Physics* **34**, R23-R53 (2001).

50 Pylkki, R. J., Moyer, P. J. & West, P. E. SCANNING NEAR-FIELD OPTICAL MICROSCOPY AND SCANNING THERMAL MICROSCOPY. *Jpn. J. Appl. Phys. Part 1 - Regul. Pap. Short Notes Rev. Pap.* **33**, 3785-3790 (1994).
51 Dobson, P. S., Weaver, J. M. R., Mills, G. & Ieee. in *2007 Ieee Sensors, Vols 1-3 IEEE Sensors* 708-711 (Ieee, 2007).
52 Tsuji, T. *et al.* Evaluation of domain boundary of piezo/ferroelectric material by ultrasonic atomic force microscopy. *Jpn. J. Appl. Phys. Part 1 - Regul. Pap. Short Notes Rev. Pap.* **43**, 2907-2913, doi:10.1143/jjap.43.2907 (2004).
53 Hinz, M., Marti, O., Gotsmann, B., Lantz, M. A. & Durig, U. High resolution vacuum scanning thermal microscopy of HfO2 and SiO2. *Applied Physics Letters* **92**, 3, doi:043122

10.1063/1.2840186 (2008).
54 Kim, K., Chung, J., Hwang, G., Kwon, O. & Lee, J. S. Quantitative Measurement with Scanning Thermal Microscope by Preventing the Distortion Due to the Heat Transfer through the Air. *Acs Nano* **5**, 8700-8709, doi:10.1021/nn2026325 (2011).
55 Luo, K., Lederman, M. & Majumdar, A. Liquid-film-mediated scanning thermal microscopy of a magnetoresistive reading head. *Microscale Thermophysical Engineering* **1**, 333-345 (1997).
56 Zabel, H. Phonons in layered compounds. *Journal of Physics-Condensed Matter* **13**, 7679-7690, doi:10.1088/0953-8984/13/34/313 (2001).
57 Greffet, J. J. & Carminati, R. Image formation in near-field optics. *Progress in Surface Science* **56**, 133-237, doi:10.1016/s0079-6816(98)00004-5 (1997).
58 Barrat, J. L. & Chiaruttini, F. Kapitza resistance at the liquid-solid interface. *Mol. Phys.* **101**, 1605-1610, doi:10.1080/0026897031000068578 (2003).
59 Cahill, D. G. *et al.* Nanoscale thermal transport. *Journal of Applied Physics* **93**, 793-818, doi:10.1063/1.1524305 (2003).
60 Koh, Y. K., Bae, M. H., Cahill, D. G. & Pop, E. Heat Conduction across Monolayer and Few-Layer Graphenes. *Nano Letters* **10**, 4363-4368, doi:10.1021/nl101790k (2010).
61 Janovjak, H., Struckmeier, J. & Muller, D. J. Hydrodynamic effects in fast AFM single-molecule force measurements. *Eur. Biophys. J. Biophys. Lett.* **34**, 91-96, doi:10.1007/s00249-004-0430-3 (2005).
62 Horcas, I. *et al.* WSXM: A software for scanning probe microscopy and a tool for nanotechnology. *Review of Scientific Instruments* **78**, doi:013705

10.1063/1.2432410 (2007).

Nanoscale resolution immersion scanning thermal microscopy

SUPPLEMENTARY INFORMATION.

Peter D. Tovee and Oleg V. Kolosov.

Physics Department, Lancaster University, Lancaster, LA1 3BE, UK.

Note 1. Finite element modeling of SThM response in air and liquid. Finite element analysis (FE) using COMSOL Multiphysics was used for both exploring the feasibility of the immersion SThM (iSThM) approach, and, after such feasibility was experimentally confirmed, for comparison of SThM response of Al/BCB and graphene/SiO_2 for in-air and iSThM images. The simulation consisted of two parts; an electrical model responsible for the electric current flow in the probe, and a thermal module dealing with the Joule heating and heat propagation through the system. A fixed potential of 0.5 V was applied to the terminals of Pd heater with all other boundaries set to be electrically insulating. The thermal module used Fourier diffusive heat equations for thermal transport in material and Joule heating in the tip. As described elsewhere[1] due to minimal dimensions used in the modeling on the order of 50 nm that exceeded or being equal to the mean-free-path (MFP) of heat carriers in the most parts of the system, such approach was appropriate. In thermal module, all inner boundaries were assigned continuity conditions, with outer sides of the air/liquid block, the sample and base of the cantilever legs set to a fixed 293 K ambient temperature. With this approach the whole 3D system could be modeled and the parameters varied as desired[2]. A material of the block encasing the whole cantilever and sample

could be changed between air, dodecane and vacuum, the tip-surface distance and tip-sample position were also independently changeable.

Note 2. Simulation of SThM response to tip-surface distance and lateral profiles in SThM. Due to the higher thermal conductivity of dodecane compared with air, true materials sensitive non-contact scanning with nanoscale resolution – a *holy grail* of SPM approaches, is expected to be possible. With the aid of the simulations a hovering contact of up to 25 nm was compared with the full contact and the temperature drop shown in table 1 in the manuscript. Lateral resolution is another very important measure for SThM probes that has been explored experimentally and using the models in this study. Simulations for samples of Al/BCB and graphene flake/Si were created for both air and liquid. Temperatures were taken at intervals up to 500 nm either side of the boundary with interval spacing closer near the boundary. Due to the large difference in thermal conductivities of the two materials there was a clear transition over the border with a resolution of approximately 50 nm. For graphite flake simulations we used 100 nm thick layer of graphite similar to the experiment. Its in-plane thermal conductivity was assumed to be 1000 times larger than perpendicular to the plane.[3] The model consisted of a Si sample block with the graphite flake on top and the sample moved with respect to the tip. As the tip made contact with the side of the flake it was then raised up and moved across the top of the flake. This allowed us to simulate the real tip's motion and also to observe the effect of side contact with the graphite flake, which may reflect higher in-plane thermal conductivity of graphite resulting in a drop in temperature observed in figure 6c in the manuscript. It is notable that both in the experiment and simulation we observed only minor difference in SThM signal on the top of the flake and Si sample that reflects low thermal conductivity of graphite perpendicular to the atomic planes.

Analytical model of the heat transport in iSThM - heat transport via cantilever *vs* heat losses to the ambient environment.

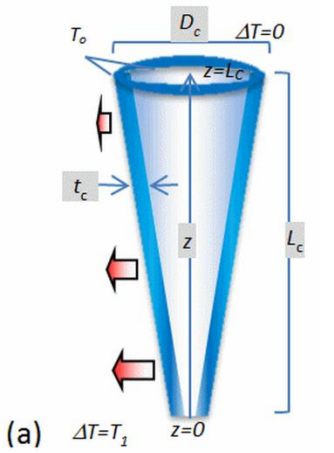

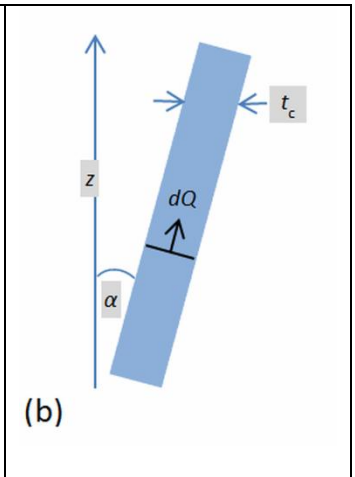

Figure S1. Equivalent analytical model of SThM sensor. (a) Schematics of the axi-symmetrical equivalent of the SP SThM probe. (b) Radial cross-section of the cantilever, t_C cantilever thickness, L_C length of the cantilever triangular section, πD_C – length of the base of triangular section, T_0 room temperature, α the cone angle and Q the heat flux down the cone wall.

As mentioned in the paper, a flat triangular geometry of the end section of the probe, fixed T at its base (close to ambient temperature due to Au leads acting as a heatsink), and evenly distributed resistive heater-sensing element along the probe, allowed to create equivalent axisymmetric model of the probe that can be evaluated analytically. These allowed to create equivalent axially symmetrical conical shell, setting thickness of the cone equal to the thickness of Si_3N_4 probe t_c, cone half-opening angle α such that the circumference of the cone base is equal to the width w_c of the triangular end section of the probe, and the height of the cone L_C is equal to the length of the triangular section. That gives $\alpha = \arcsin\left[w_c/(2\pi L_c)\right]$ with α in our case of 19.7° making the equivalent geometry shaped as a narrow angle cone.

At first we calculate the thermal resistance to the base of the cantilever in a vacuum where heat is transported exclusively through the cantilever. We note that the heater in the original sensor has approximately constant width along the sensor height[4], resulting in constant heating per unit height of its equivalent cone. Defining z as position along the cone with 0 at the tip and L_C at the base of the triangle, the heat generated from $z = 0$ to z can be written as $Q_z = zQ/L_C$, where Q is the total Joule heat generated in the probe. This heat flows through the ring-shaped cross-section of the cone with the area $2\pi z(\tan\alpha)t_C$ where t_C is the cantilever thickness creating heat flux $\frac{Qz}{2\pi zL_C(\tan\alpha)t_C} = \frac{Q}{2\pi L_C(\tan\alpha)t_C}$. This heat generates a temperature gradient $\frac{dT}{dz} = \frac{1}{k_c}\frac{Q}{2\pi L_C(\sin\alpha)t_C}$, where k_c is the thermal conductivity of the cantilever. One can note that the temperature gradient does not depend on z and therefore is constant along the cantilever, with the temperature difference between cantilever tip and its base $\Delta T = \frac{1}{k_c}\frac{Q}{2\pi L_C(\sin\alpha)t_C}$. This conclusion is very similar to the FEA simulations for the original 3D geometry of the SP SThM probe we have done in our previous work[2] showing approximately linear drop of the temperature along the triangular section of the SThM cantilever, therefore supporting approximations we used in this analytical model. The corresponding thermal resistance of the cantilever flux to the base is then

$$R_b = \frac{\Delta T}{Q} = \frac{1}{2\pi t_C k_c \sin\alpha} \quad (1)$$

We can also estimate the heat transport through the ambient environment (air or liquid) by considering the cone as a series of sections dissipating the heat to the environment. The flux per unit area emitted by the section of the cone at position z with section diameter $d = 2z\tan(\alpha)$ and

height *dz* can be estimated by assuming that it is similar to the flux from the sphere of same diameter. Although such consideration is clearly an approximation, it will allow us to compare the various components of heat transport in iSThM. The total heat flux from such a sphere to the media per unit area is $Q_m = \frac{2T_z k_m}{d}$ where k_m is the heat conductivity of the media[5]. The section of the cone has the area on both sides of the cone $dA = 2\pi d \frac{dz}{\cos\alpha}$, producing flux $dQ_m = \frac{2T_z k_m}{d}\frac{2\pi d}{\cos\alpha}dz = \frac{4\pi T_z k_m}{\cos\alpha}dz$. We can see that the heat flux to the media per unit distance along the cone (cantilever) is independent on the position *z* (one can note that the increase of the area losing heat was compensated by the lower heat loss efficiency per unit area for the section with the larger diameters) and depends solely on the local temperature T_z. Assuming that in each section the heat flow through the cantilever to the base dominates, we can assume the linear temperature dependence as a function of *z*. Then $T_z = \Delta T\,(L_C - z)/L_C$ and integrating *dQ* over *z* from 0 to L_C, we obtain that the heat flux $Q = \Delta T \frac{2\pi k_m L_C}{\cos\alpha}$ and the corresponding thermal resistance

$$R_m = \frac{\cos\alpha}{2\pi k_m L_C} \tag{2}$$

It is useful also to find a ratio of thermal resistances to the medium R_m to thermal resistance to the base R_b by $R_m/R_b = \frac{2\pi t_C k_c \cos\alpha \sin\alpha}{2\pi k_m L_C} = \sin\alpha\cos\alpha\frac{t_C}{L_C}\frac{k_c}{k_m}$. This value is dimensionless and indicates that the share of the heat flux to the media (inverse to the corresponding thermal resistance) is linearly increased with both the length of the cantilever and the heat conductivity of

the media. Combining equations (1) and (2) together we can estimate the total thermal resistance R_t to the base using law of parallel resistances[6,7] as $R_t = R_b R_m / (R_b + R_m)$.

It should be noted that if the heat losses to the ambient environment started to dominate, the result will be a sharper drop of temperature with increase of distance from the tip apex. This, in turn, would additionally concentrate the heat nearer to the tip apex, that would lead to further increase of the iSThM spatial resolution.

Note 3. Experimental and simulation comparison between performance of dopped Si (DS)[8] and Si_3N_4 with resistive Pd sensor (SP)[4] probes. Before the Si_3N_4 SThM probes were selected as iSThM probes, two other types of probes were investigated. Initially Wollaston wire (WW) probes were used to test the validity of scanning in liquid since WW probes are more robust. They were immersed in liquid and used on a sample of few tens of nm exfoliated graphite flakes on the glass slide. It was found that WW had no only a poor resolution due to the probe's large tip contact area, but, more essential, thermal response dominated by the overall probe distance to the sample surface, rather than sample thermal properties. The microfabricated dopped Si (DS) probes (Anasys Instruments, USA) were also tested in a modified Topometrix and in Multimode AFM (Bruker, Germany) using an underliquid cell capable of holding the thermal probes. The DS probes were used with the multi-mode system to image graphene flake on glass, and an image of this can be seen in figure S2.

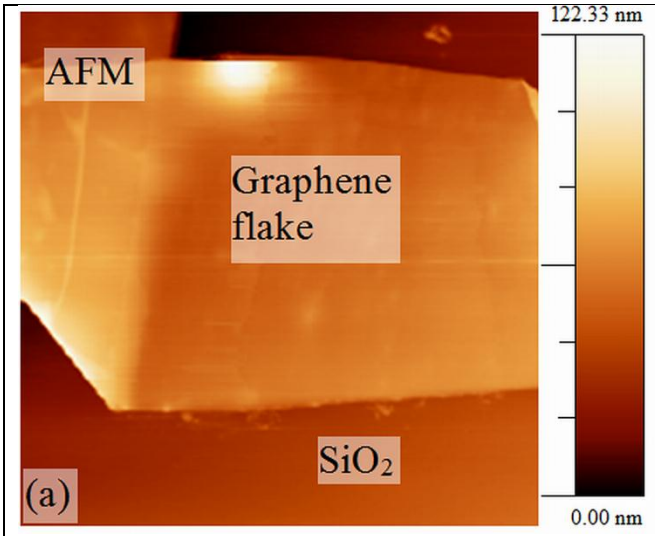

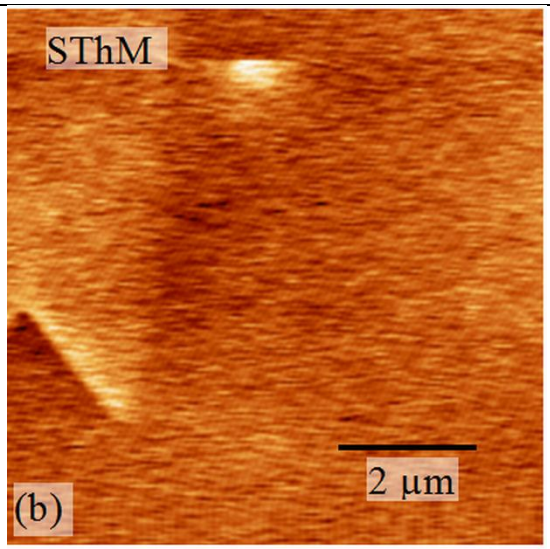

Figure S2. SThM of graphene on glass in liquid using the DS probe showing (a) AFM height image and (b) thermal image.

It is clear from Fig. S2 that the DS probe was also not sensitive to the change in thermal conductivity between the graphene and glass, but reflecting mainly topographical changes rather than thermal properties of the sample. This made us to conclude that the thermal sensor positioned at the end of the cantilever and far from the tip apex is detrimental to iSThM operation, while its operation in vacuum could be quite successful[9]. The SP probes which have their heater much closer to the tip apex and therefore the sample surface turned out to be far more sensitive to the changes in surface thermal conductivity in iSThM and therefore are preferred way for thermal scanning in liquids. We believe that future designs of optimal SThM probes, should have similar design, that may include compatible materials allowing to operate in polar liquids such as water or electrolytes.

Note 4. Electronics setup for experimental iSThM measurements. In the measurements, Maxwell bridge (Fig. S3) is balanced at room temperature and absence of AFM laser

illumination before imaging. The measurements are performed at 91 KHz AC modulation and DC offset that defines the initial temperature of the sensor.

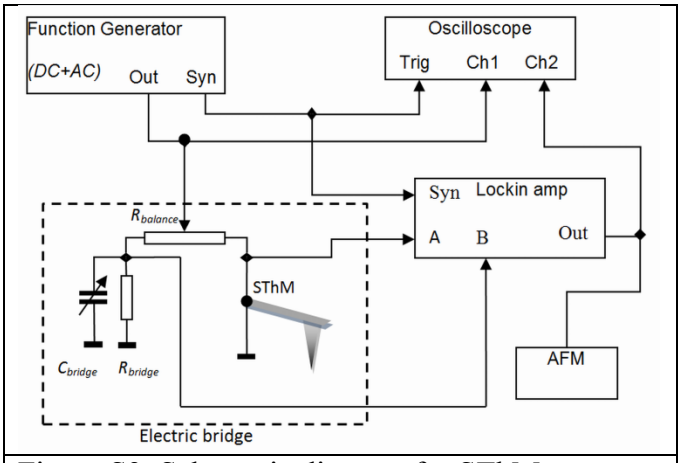

Figure S3. Schematic diagram for SThM measurement electronics including the Maxwell electrical bridge (box marked with dashed outline) used to measure the change in probe resistance. The generator applied a DC voltage with AC detection signal at 91 kHz.

REFERENCES

1 Majumdar, A., Carrejo, J. P. & Lai, J. THERMAL IMAGING USING THE ATOMIC FORCE MICROSCOPE. *Applied Physics Letters* **62**, 2501-2503, doi:10.1063/1.109335 (1993).

2 Tovee, P., Pumarol, M. E., Zeze, D. A., Kjoller, K. & Kolosov, O. Nanoscale spatial resolution probes for Scanning Thermal Microscopy of solid state materials. *J. Appl. Phys.* **112**, 114317 (2012).

3 Paronyan, T. M., Pigos, E. M., Chen, G. G. & Harutyunyan, A. R. Formation of Ripples in Graphene as a Result of Interfacial Instabilities. *Acs Nano* **5**, 9619-9627, doi:10.1021/nn202972f (2011).

4 Dobson, P. S., Weaver, J. M. R., Mills, G. & Ieee. in *2007 Ieee Sensors, Vols 1-3 IEEE Sensors* 708-711 (Ieee, 2007).

5 Lienhard, J. H. *A Heat Transfer Textbook*. (Phlogiston Press, 2008).

6 Majumdar, A. Scanning thermal microscopy. *Annu. Rev. Mater. Sci.* **29**, 505-585 (1999).

7 Pumarol, M. E. *et al.* Direct Nanoscale Imaging of Ballistic and Diffusive Thermal Transport in Graphene Nanostructures. *Nano Letters* **12 (6)**, 2906–2911, doi:10.1021/nl3004946 (2012).

8 King, W. P. & Goodson, K. E. Thermal writing and nanoimaging with a heated atomic force microscope cantilever. *Journal of Heat Transfer-Transactions of the Asme* **124**, 597-597, doi:10.1115/1.1502634 (2002).

9 Hinz, M., Marti, O., Gotsmann, B., Lantz, M. A. & Durig, U. High resolution vacuum scanning thermal microscopy of HfO2 and SiO2. *Applied Physics Letters* **92**, 3, doi:043122
10.1063/1.2840186 (2008).